Biological response to intensified upwelling and to a river plume in the northeastern South China Sea: A modeling study

Jianping Gan,[1,2] Zhongming Lu,[2] Minhan Dai,[3] Anson Y. Y. Cheung,[2] Hongbin Liu,[2] and Paul Harrison[2]

Received 12 June 2009; revised 11 March 2010; accepted 7 April 2010; published 2 September 2010.

[1] A coupled three-dimensional physical model and a nitrogen-based dissolved inorganic nitrogen, phytoplankton, zooplankton, and detritus (NPZD) ecosystem model was used to study the ecosystem responses to the wind-driven summer upwelling and to the Pearl River plume over a distinctly widened shelf in the northeastern South China Sea (NSCS). Forced with an idealized, but representative, upwelling-favorable wind and the river discharge for the purpose of process-oriented study, we identified two high chlorophyll centers that are typically observed over the NSCS shelf and stimulated by nutrient enrichment from intensified upwelling over the widened shelf and from the river plume. The nutrient enrichment has strong along-shore variability involving the variable cross-isobath nutrient transport between the middle and the inner widened shelf during the upwelling and an eastward expansion of the nutrient-rich plume. About 20% of the upwelled nutrient-rich deep water from the outer shelf reaches the inner shelf where algal blooms occur. Nutrient enrichment in the plume stretches over a broad extent of the shelf and produces significant biomass on the NSCS shelf. The plume is physically governed by intensified surface Ekman dynamics that leads to a strong offshore nutrient transport and eventually offsets the shoreward transport caused by the upwelling in the NSCS. Biological forcing and circulation dynamics of the surface Ekman layer jointly form the spatial dislocation and temporal variation of NO_3, phytoplankton, and zooplankton biomasses in the upwelled and plume waters. The simulated results qualitatively resemble field and satellite measurements and demonstrate the physically modulated biological responses to the intensified upwelling and plume-influenced NSCS shelf.

Citation: Gan, J., Z. Lu, M. Dai, A. Y. Y. Cheung, H. Liu, and P. Harrison (2010), Biological response to intensified upwelling and to a river plume in the northeastern South China Sea: A modeling study, *J. Geophys. Res.*, *115*, C09001, doi:10.1029/2009JC005569.

1. Introduction

[2] Coastal upwelling is one of the most prominent physical processes linking wind-driven currents and shelf topography and is commonly characterized by the formation of strong alongshore coastal currents and upward motion induced by the offshore mass transport at the surface and the onshore mass transport in the deep layers. By transporting deep water with a high concentration of nutrients to the euphotic zone for a potential phytoplankton bloom, the coastal upwelling significantly modulates the biogeochemistry and biological productivity of coastal water. Moreover, coastal waters are also the transition zone between land and open ocean where terrestrial nutrient and buoyancy inputs by river discharge stimulate algal blooms and alter the flow field, respectively.

[3] The shelf topography over the broad continental shelf in the northeastern South China Sea (NSCS) is characterized by a highly variable coastline with many estuaries, bays, and coastal capes, and most distinctly by the existence of a prominent eastward widened shelf (Figure 1). An abrupt offshore shift of isobaths east of the Pearl River Estuary (PRE) forms the widened shelf region. It is bounded by the 50 m isobath at its southern edge and has shoreward convex isobaths that converge at its head about one-half degree southwest of Shanwei. Forced by the prevailing southwesterly winds in summer, cold deep water upwells to the surface layer over the NSCS shelf [*Gan et al.*, 2009a]. In addition, fresh water from the Pearl River (PR) spreads over the shelf by the upwelling coastal jet and forms an elongated river plume over the NSCS shelf [*Gan et al.*, 2009b].

[4] NSCS is part of the oligotrophic South China Sea (SCS) with extremely low nutrient concentrations in the surface water and very low levels of phytoplankton biomass and

[1]Department of Mathematics, Hong Kong University of Science and Technology, Kowloon, Hong Kong.
[2]Division of Environment, Hong Kong University of Science and Technology, Kowloon, Hong Kong.
[3]State Key Laboratory of Marine Environmental Science, Xiamen University, Xiamen, China.

0148-0227/10/2009JC005569

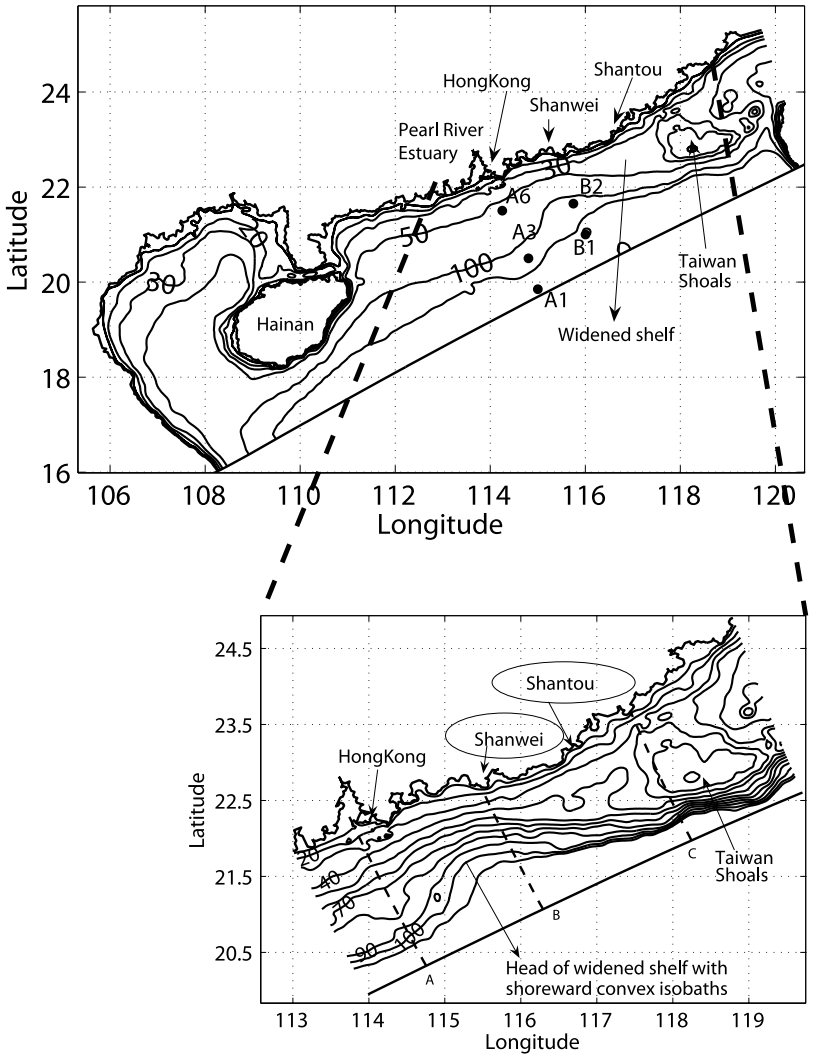

Figure 1. The topography (in meters) in the northern South China Sea and the zoomed area in the region between Guangdong and Xiamen. The selected cross-shelf sections (dashed lines) are marked by lines A, B, and C, and survey stations are marked by solid circles. The location of shoreward convex isobaths exists at the head of the widened shelf about half degree southwest of Shanwei.

productivity. In general, it is *N* limited [*Chen et al.*, 2004; *Wu et al.*, 2003; *Zhang et al.*, 1999], but it is likely *P* limited in the waters in the estuary where excess nitrate from the PR discharges onto the shelf [*Ning et al.*, 2004; *Yin,* 2002; *Yin et al.*, 2004; *Xu et al.*, 2008]. A strong subsurface chlorophyll maximum (SCM) is a common phenomenon in the SCS [*Liu et al.*, 2002; *Ning et al.*, 2004; *Lu et al.*, 2010]. In summer, phytoplankton and zooplankton blooms occur in the nearshore waters of the NSCS because of the nutrient enrichment caused by wind-driven coastal upwelling [*Liu et al.*, 2002; *Ning et al.*, 2004]. Phytoplankton blooms in the river plume have been frequently reported [*Yin et al.*, 2004; *Xue and Chai*, 2001; *Dai et al.*, 2008] and significant spatial variability of the pelagic ecosystem has been observed [*Harrison et al.*, 2008; *Huang et al.*, 2008; *Li et al.*, 2006]. However, time-dependent three-dimensional responses of the ecosystem to distinct wind-driven coastal upwelling circulation and associated plume dynamics in the NSCS have not been studied. The respective contribution of the upwelled and plume waters to the plankton biomass on the shelf resulting from coupled physical-biological processes remains largely unknown.

[5] Coupled physical-biological modeling is an efficient approach to compensate for temporally and spatially limited measurements. A relatively simple ecological model has proved to be sufficient to conceptually understand the simple trophic linkages with circulation [e.g., *Spitz et al.*, 2005; *Powell et al.*, 2006]. *Xue and Chai* [2001] used a coupled physical-biological model, with two sizes of phytoplankton and zooplankton, to investigate nutrient and plankton dynamics in the PRE. *Liu et al.* [2002, 2007] used a coupled three-dimensional circulation and four-compartment NPZD biological model to simulate the seasonal and spatial variability of chlorophyll and primary production in the SCS basin. There are very few studies over the continental shelf in the NSCS that have investigated coupled physical-biological effects by either field observations or modeling. This study utilizes a three-dimensional, coupled physical and nitrogen-based ecosystem model and a combination of available in situ

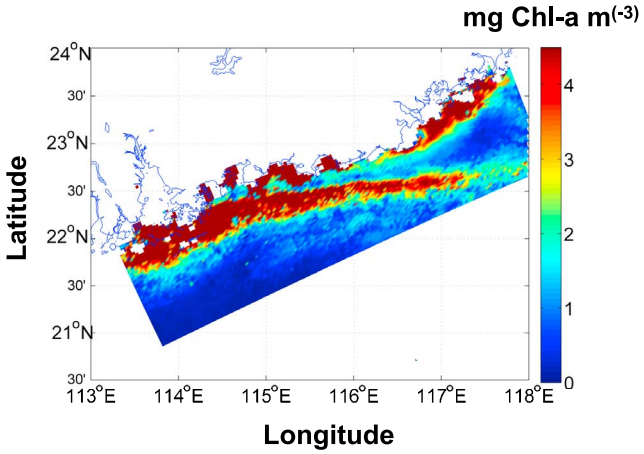

Figure 2. MODIS sea surface chlorophyll-*a* (mg Chl-*a* m^{-3}) distribution in the NSCS, averaged from 29 June 2003 to 7 July 2003.

measurements and satellite-derived data to investigate the time-dependent three-dimensional biological response to nutrient enrichment by coastal upwelling circulation and associated Pearl River plume dynamics over the shelf of the NSCS.

2. Observational Features

[6] Satellite-derived high-resolution (1 km) of surface chlorophyll from the Moderate Resolution Imaging Spectroradiometer (MODIS) and in situ measurements are shown in Figures 2, 3, and 4. Field measurements of salinity, temperature, and chlorophyll-*a* were made by an SBE-19-plus Conductivity–Temperature–Depth/Pressure (CTD) unit aboard the R/V Yanpin II during two cruises in 2004 and one cruise in 2008 of the upwelling season. Discrete samples for NO_3 were collected using a Rosette sampler with Go-flo bottles (General Oceanics Co.). Nitrate was determined colorometrically using a flow injection analyzer (Tri-223 autoanalyzer) and chlorophyll-*a* was determined using the standard fluorometric method [*Parsons et al.*, 1984].

[7] Figure 2 shows the average sea surface chlorophyll distribution in the NSCS derived from MODIS data from 29 June to 7 July 2003, during which time wind forcing was dominated by upwelling-favorable winds but interrupted periodically by upwelling-relaxing or downwelling–favorable winds. Two distinct high-chlorophyll concentrations coexisted over the NSCS shelf. The one over the inner shelf in the eastern part of the NSCS resulted from an intensified upwelling induced by local shelf topography [*Gan et al.*, 2009a], and the other one in the freshwater plume stretched from the PRE over the middle shelf and formed a long tongue-shaped phytoplankton bloom. The nutrient in the plume originated from the high concentrations of nutrients in the river discharge and was driven eastward by coastal upwelling currents. The nutrient input from coastal upwelling and from the river discharge were clearly the two major controlling factors of the pelagic ecosystem in the NSCS during the southwest monsoon. Generally, low chlorophyll was found in the other NSCS regions not affected by upwelling or by the plume, indicating the oligotrophic characteristics of the SCS.

[8] SCS Coastal Process Experiment (SCOPE) is a multidisciplinary research project designed to understand biogeochemical dynamics in the wind-driven coastal circulation on the continental shelf in the SCS. Figure 3 shows salinity and chlorophyll from a calibrated SBE917 CTD as well as NO_3 at 5 m measured during SCOPE. Qualitatively similar to that in Figure 2, field measurements confirm two distinct high-chlorophyll centers that coexisted in the plume and in the intensified upwelling off Shantou.

[9] Depth-dependent features of the chlorophyll distribution are shown by the cross-shelf section A, near the entrance

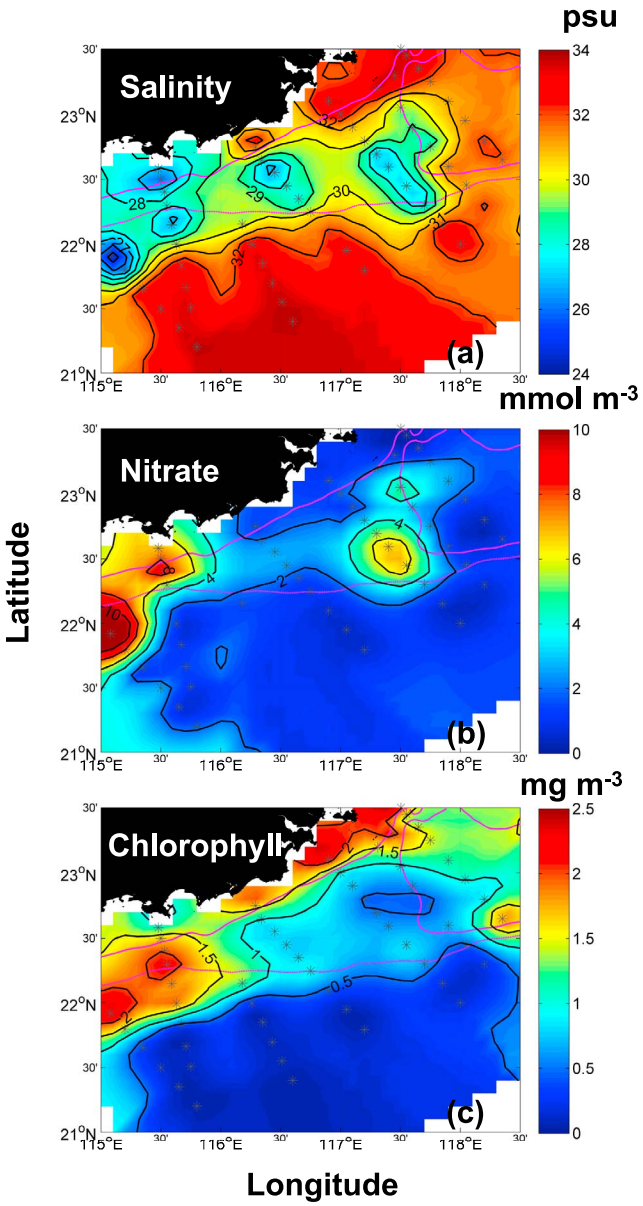

Figure 3. Ensembles of (a) salinity (psu), (b) NO_3 (mmol m^{-3}), and (c) chlorophyll (mg m^{-3}) at 5 m from a field measurement conducted during the summer upwelling season of 29 June 2008 and 16 July 2008. The pink solid and dashed lines refer to the 30 m and 50 m isobaths, respectively.

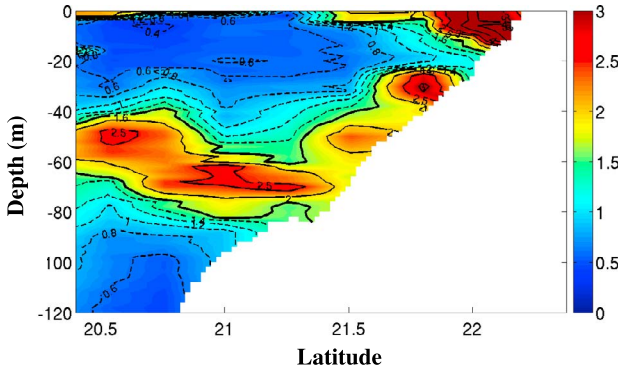

Figure 4. Observed chlorophyll-*a* (mg Chl-*a* m^{-3}, CTD fluorescence probe) of section A during 20–21 July 2004.

of the PRE in Figure 4. Distinct high-chlorophyll concentrations existed in both the surface and subsurface at depths of about 50 m due to the nutrient supplies from the river plume and formation of the subsurface chlorophyll maximum (SCM) [*Lu et al.*, 2010], respectively. They also occurred over the slope near the bottom due to the up-slope nutrient advection in the upwelling. The plume-induced algal bloom reached a depth of about 20 m in the nearshore, extended seaward, and shoaled offshore. High-chlorophyll concentrations in SCM varied between 30 and 70 m and extended from nearshore waters to deeper waters offshore (Figures 4 and 5). During the sampling period, the wind over section A was downwelling favorable. The blooms over the inner shelf were likely retreating from previous upwelling. Section B was sampled during upwelling-favorable winds and only three profiles were measured. In general, the observed profiles in Figure 5 exhibited very low chlorophyll concentrations (~0.1 mg m^{-3}) at the surface, as a result of the oligotrophic SCS. Low chlorophyll extended to 30 m but increased sharply at the maximum in SCM. The chlorophyll concentration decreased gradually in deeper waters and disappeared at a depth of about 100 m. NO_3 was nearly undetectable down to 30 m and increased linearly below that depth. Similar vertical distributions of chlorophyll in the NSCS have been reported previously. During an investigation after a period of upwelling-favorable winds, the surface chlorophyll in the NSCS ranged from 1.0–4.0 μg L^{-1}, with high nearshore concentrations that decreased offshore [*Cai et al.*, 2002]. They also identified a significant SCM with an average value of 3.2 μg L^{-1} at a depth of 50–75 m.

[10] There have been few studies on zooplankton biomass in the NSCS. According to a time-series study of coastal waters outside Hong Kong, the yearly average phytoplankton biomass was about 1.3 mmol N m^{-3}, and the zooplankton biomass was 0.34 mmol N m^{-3}, with a zooplankton to phytoplankton ratio of about 0.3 (H. B. Liu, unpublished data, 2009). Another study on zooplankton biomass in Daya Bay, east of Hong Kong, reported an annual range in zooplankton biomass of 0.24–0.61 mmol N m^{-3} [*Du et al.*, 2006].

3. The Model and Its Implementation

[11] Numerical modeling provides a dynamic interpolation or extrapolation of spatially and temporally limited field measurements. A three-dimensional, coupled, physical-biological model is used to simulate the ecosystem response to the wind-driven summer upwelling over the continental shelf in the NSCS. The physical and biological models and their implementation are described below.

3.1. Physical Model

[12] We used the Regional Ocean Model System (ROMS) [*Shchepetkin and McWlliams*, 2005] for three-dimensional, time-dependent, oceanographic flows governed by hydrostatic primitive equations. A local closure scheme, based on level-2.5 turbulent kinetic energy equations [*Mellor and Yamada*, 1982], was adopted in the vertical mixing parameterization. The model domain extends from 15.99°N, 108.17°E in the southwest corner to about 25.81°N, 119.54°E in the northeast corner with its central axis directed 23° anticlockwise from true east (Figure 1). A curvilinear grid

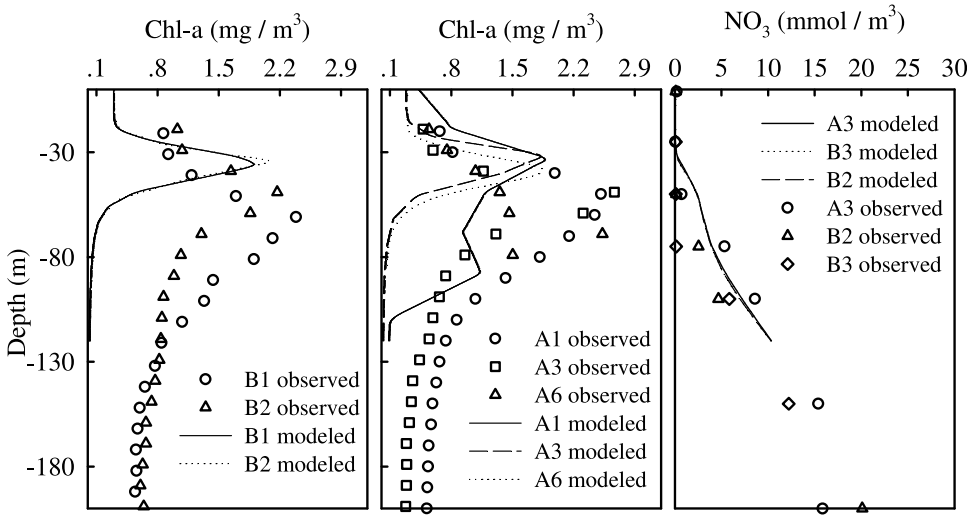

Figure 5. Chlorophyll profiles (open circles, squares, and triangles) observed in section A and section B and the corresponding modeled profiles (curves) on day 30 at the same stations. The locations of the sampling stations are marked in Figure 1.

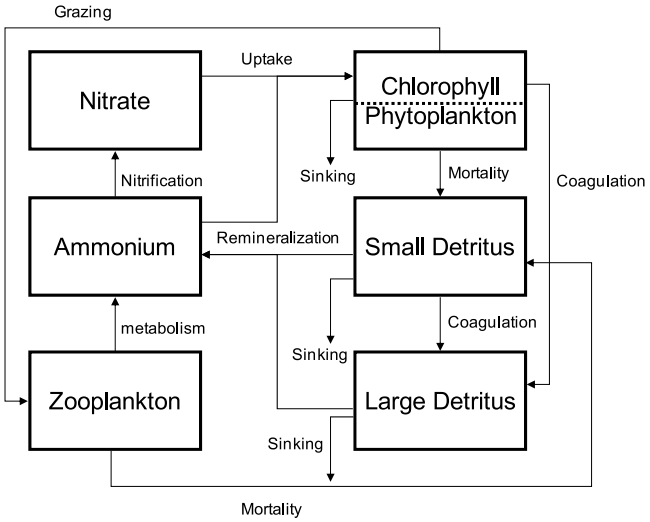

Figure 6. Biological model schematic.

with a (450,140) dimensional array was adopted for horizontal coordinates (x, y) that formed a 3 km horizontal grid size on average. The stretched, generalized, terrain-following, s-coordinate [*Song and Haidvogel*, 1994] was adopted for the vertical coordinates. $\theta_s = 2.5$ and $\theta_b = 0.8$ were used in s to give a higher vertical resolution in the surface and the bottom boundary layers. The model has 30 vertical levels that form a minimum grid spacing of less than 1 m in the nearshore water column and about 10 m over the outer shelf. The water depth, $h(x, y)$, was obtained by merging ETOPO2 (1/30°) from the National Geophysical Data Center (USA) and by digitizing depths from navigation charts published by China's Maritime Safety Administration. The minimum water depth was set equal to 5 m, and the topography was smoothed slightly to reduce truncation errors. In order to clearly identify the underlying processes and mechanisms in the biological responses to upwelling and river discharge over the shelf in NSCS, these responses and associated processes were studied as if they were isolated from forcing of the outer ocean. In this coupled physical and biological simulation, upwelling was assumed to be driven entirely by a spatially uniform southwesterly wind stress (0.025 Pa) to represent the typical NSCS upwelling conditions in the summer. The model was initialized with horizontally uniform temperature and salinity profiles obtained from field measurements at station A3 (Figure 1) that resemble the climatological data for July [*Boyer et al.*, 2005]. The velocities and surface elevations were initialized to zero. The model domain has two open boundaries on which open boundary conditions (OBCs) [*Gan and Allen*, 2005] favorable for simulating shelf circulation were applied. The discharge rate for the Pearl River was set equal to the typical summer value of 16,500 $m^3\ s^{-1}$, and the salinity, temperature, and NO_3 of the river were set to 10, 29.5°C, and 60 mmol m^{-3}, respectively, in the entire water column at the head of the PRE. The buoyancy flux from the atmosphere was set equal to zero for simplicity. The model was run for 30 days. Daily-averaged outputs are used in the analyses. More details about the model can be found in *Gan et al.* [2009a, 2009b] in which the model was shown to successfully capture the observed coastal upwelling over the unique widened shelf and the upwelling-plume interaction in the NSCS.

3.2. Biological Model

[13] The biological model over the continental shelf of NSCS is the Fasham-type ecosystem model [*Fasham et al.*, 1990] that is embedded in ROMS [*Fennel et al.*, 2006; *Hofmann et al.*, 2008]. It is a nitrogen-based ecosystem model which includes seven prognostic variables: nitrate (N), ammonium (A), chlorophyll (Chl-a), phytoplankton (P), zooplankton (Z), large detritus (LD), and small detritus (SD) (or $D = LD + SD$). A schematic diagram of the biological model is shown in Figure 6. The ecosystem model equations can be written as:

$$\frac{\partial [N]}{\partial t} = -\mu_{\max} * f(I) * \frac{[N]}{k_N + [N]} * \frac{1}{1 + [A]/k_A} * [P] + n * [A], \quad (1)$$

$$\frac{\partial [A]}{\partial t} = -\mu_{\max} * f(I) * \frac{[A]}{k_A + [A]} * [P] - n * [A] + l_{BM} * [Z] + L_E * \frac{[P]^2}{k_P + [P]^2} * AE_N * [Z] + r_{SD} * [SD] + r_{LD} * [LD], \quad (2)$$

$$\frac{\partial [P]}{\partial t} = \mu * [P] - m_P * [P] - \tau * [SD + P] * P - g_{\max} * \frac{[P]^2}{k_P + [P]^2} * [Z] - w_P \frac{\partial [P]}{\partial z}, \quad (3)$$

$$\frac{\partial [Z]}{\partial t} = g_{\max} * \frac{[P]^2}{k_P + [P]^2} * AE_N * [Z] - l_{BM} * [Z] - L_E * \frac{[P]^2}{k_P + [P]^2} * AE_N * [Z] - m_Z * [Z]^2, \quad (4)$$

$$\frac{\partial [SD]}{\partial t} = g_{\max} * \frac{[P]^2}{k_P + [P]^2} * (1 - AE_N) * [Z] + m_Z * [Z]^2 + m_P * [P] - \tau * ([SD] + [P]) * [SD] - r_{SD} * [SD] - w_{SD} \frac{\partial [SD]}{\partial z}, \quad (5)$$

$$\frac{\partial [LD]}{\partial t} = \tau * ([SD] + [P])^2 - r_{LD} * [LD] - w_{LD} * \frac{\partial [LD]}{\partial z}. \quad (6)$$

[14] The growth rate of phytoplankton, μ and expressions of $f(I)$ and $\mu_{\max}$ are presented in Appendix. The variable n in equations (1) and (2) is the nitrification rate that is regulated by light [*Olson*, 1981].

[15] Because pelagic ecosystem studies in the NSCS are relatively limited, most of the biological parameters applied in the biological model were taken from ROMS [*Fennel et al.*, 2006]. All the biological parameters are listed in Table 1 and sources of the parameters can be found in *Fennel et al.* [2006] and *Spitz et al.* [2005]. The zooplankton half-saturation constant for ingestion was chosen to be $K_P = 1$ mmol N m^{-3}. From a series of experiments to test ecosystem sensitivity to the biological parameters, such as phytoplankton/zooplankton growth/grazing rate, half-saturation constants for phyto-

Table 1. Biogeochemical Model Parameters

Description	Symbol	Value	Unit
Light attenuation due to seawater	k_{water}	0.04	M^{-1}
Light attenuation by chlorophyll	k_{Chla}	0.025	$(m^2 mgChl\text{-}a)^{-1}$
Initial slope of the *P-I* curve	α	0.025	$mgC(mgChl\text{-}a Wm^{-2}d)^{-1}$
Maximum cellular chlorophyll: C ratio	θ_m	0.054	$mgChl\text{-}a(mgC)^{-1}$
Half-saturation for phytoplankton NO_3 uptake	K_N	0.5	mmol Nm^{-3}
Half-saturation for phytoplankton. NH_4 uptake	K_A	0.5	mmol Nm^{-3}
Phytoplankton mortality rate	m_P	0.15	d^{-1}
Zooplankton maximum grazing rate	g_{max}	0.6	d^{-1}
Zooplankton assimilation efficiency for nitrogen	AE_N	0.75	
Zooplankton half-saturation constant for ingestion	k_P	1	mmol Nm^{-3}
Zooplankton basal metabolism	l_{BM}	0.1	d^{-1}
Zooplankton specific excretion rate	L_E	0.1	d^{-1}
Zooplankton mortality rate	m_Z	0.025	d^{-1} (mmol $Nm^{-3})^{-1}$
Small detrital remineralization rate	r_{SD}	0.03	d^{-1}
Large detritus remineralization rate	r_{LD}	0.01	d^{-1}
Coagulation rate	τ	0.05	d^{-1}
Sinking velocity for small detritus	w_{SD}	0.1	md^{-1}
Sinking velocity for large detritus	w_{LD}	1	md^{-1}
Sinking velocity for phytoplankton	w_P	0.1	md^{-1}
Maximum nitrification rate	n_{max}	0.05	d^{-1}

plankton and zooplankton ingestion and nitrate and ammonium uptake, we found that altering these parameters within a reasonable range reported in various studies did not markedly affect the pattern of major biological response. The biological model is coupled with the physical model at identical temporal and spatial resolutions.

[16] An idealized diurnal cycle of photosynthetically active radiation (*PAR*, W m^{-2}; Appendix A) at the sea surface, was adopted in this model. The night time and daytime *PAR* (16 h) is calculated by:

$$\begin{aligned} PAR &= 450 * \sin(t * \pi/16), 1hr \le t \le 16hr \quad \text{for daytime} \\ PAR &= 0, \qquad\qquad t > 16hr \quad\quad\quad\quad \text{for night time} \end{aligned} \tag{7}$$

so the daily average value of about 190 W m^{-2} is close to the observed mean value in the NSCS.

[17] Similar to the physical variables, the initial values for biological variables were chosen to be horizontally uniform for all parameters. Nitrate and Chl-*a* observations were made aboard the *R/V* Yanpin II at station A3 during July 2000 (115.8°E, 20.1°N; Figure 1). The initial profiles for other parameters were from a one-dimensional model after a 1 year run with a small background diffusivity and without sinking of phytoplankton [*Spitz et al.*, 2005]. Since there were no available phytoplankton, zooplankton, and detritus observations, the initial values of these parameters in the one-dimensional model were calculated from chlorophyll data assuming a ratio of 1.59 and 0.70 for chlorophyll/phytoplankton, and detritus/phytoplankton, respectively [*Evans and Garcon*, 1997]. The ratio of zooplankton/phytoplankton was set equal to 0.3 according to observations beyond Hong Kong waters. A radiation boundary condition was applied to the biological variables.

4. Model Results

4.1. Characteristic Responses of the Ecosystem

[18] The simulated distributions of surface velocities and salinity (Figure 7), bottom velocities and *N* (Figure 8), and surface *N*, Chl-*a,* and *Z* (Figure 9) are illustrated for the initial stage on day 10 and the mature stage of the ecosystem response on day 30. The general flow response on the shelf to the southwesterly winds is characterized by a gradual enhancement of a coastal upwelling jet from day 10 to 30 as a result of the developing cross-shelf pressure gradient due to surface Ekman transport. The currents markedly veer offshore at the diverging isobaths over the widened shelf and bifurcate into the northern and southern components west of the Taiwan Shoals. At the bottom, currents have their strongest shoreward components near the convex isobaths at the head of the widened shelf, formed by the intensified bottom local Ekman transport and shoreward geostrophic currents [*Gan et al.*, 2009a]. The shoreward-advected deep dense water is subsequently directed eastward and forms a maximum upwelling in the lee of a coastal cape (near Shantou) as result of a local pressure gradient force [*Gan and Allen*, 2002]. The characteristic upwelling circulation largely controls the nutrient transport and shapes the distribution of biological variables in the NSCS (Figures 8 and 9). The strongest shoreward *N* transport in the bottom boundary layer occurs near the head of the widened shelf off Shanwei. This *N* flux crosses the 50 m isobath on day 10 and is subsequently directed eastward over the shelf between the 30 and 50 m isobaths by the upwelling jet. The nutrient-rich, deep water eventually upwells to the surface in the lee of the coastal cape near Shantou.

[19] In response to the upwelling circulation, freshwater discharged from the Pearl River initially forms a bulge-shaped river plume at the entrance of the PRE and subsequently spreads seaward and eastward over the shelf (Figure 7). At the same time, the upwelled, higher salinity water reaches the surface next to the coast by day 10 and extends to the entire inner shelf shoreward of the plume at the mature stage of upwelling on day 30. The simulated upwelling circulation and salinity resemble the features that are displayed in the in situ and satellite-derived measurements in Figures 2 and 3 and by *Gan et al.* [2009a, 2009b]. The high nutrient concentration in the plume (Figure 9) forms another prominent algal bloom in addition to the bloom caused by the intensified upwelling over the widened shelf in

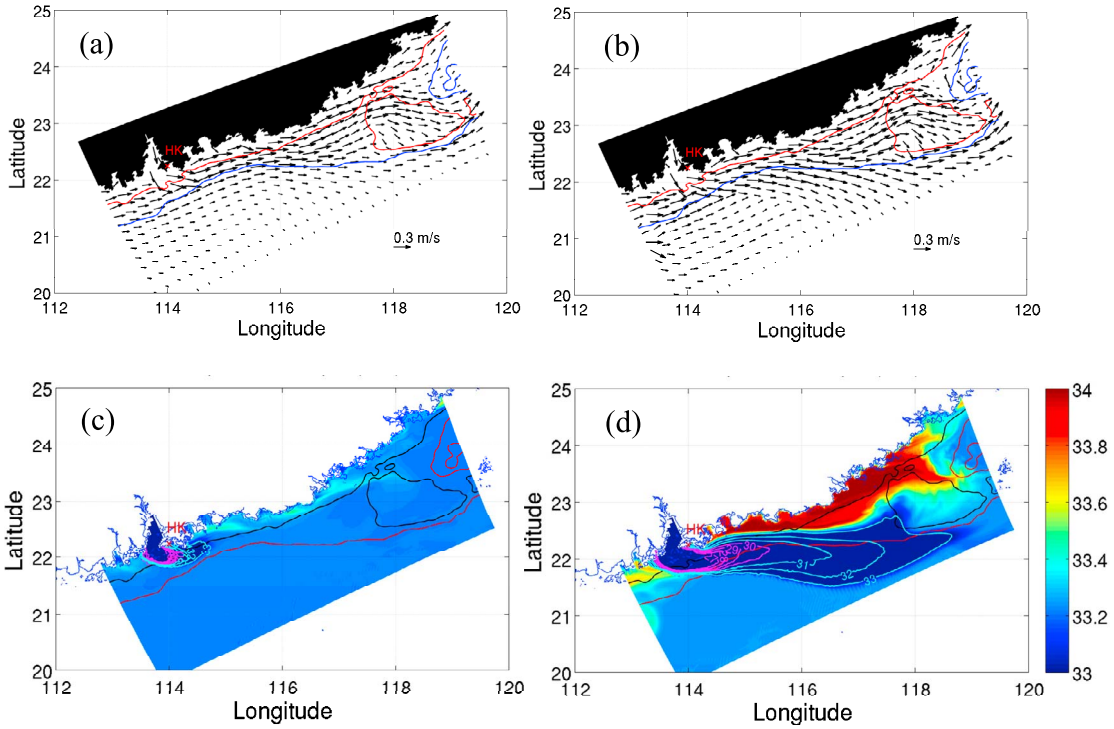

Figure 7. Surface (a and b) velocity vectors (m s^{-1}) and (c and d) salinity (psu) on days 10 (left) and 30 (right).

the NSCS. Together they shape the characteristics of the ecosystem by forming two biologically active regions over the shelf, in agreement with the chlorophyll concentrations derived from satellite data in Figure 2 and from in situ measurements in Figure 3.

[20] In general, N has much shorter alongshore and offshore extensions than the salinity field in the plume (Figure 9)

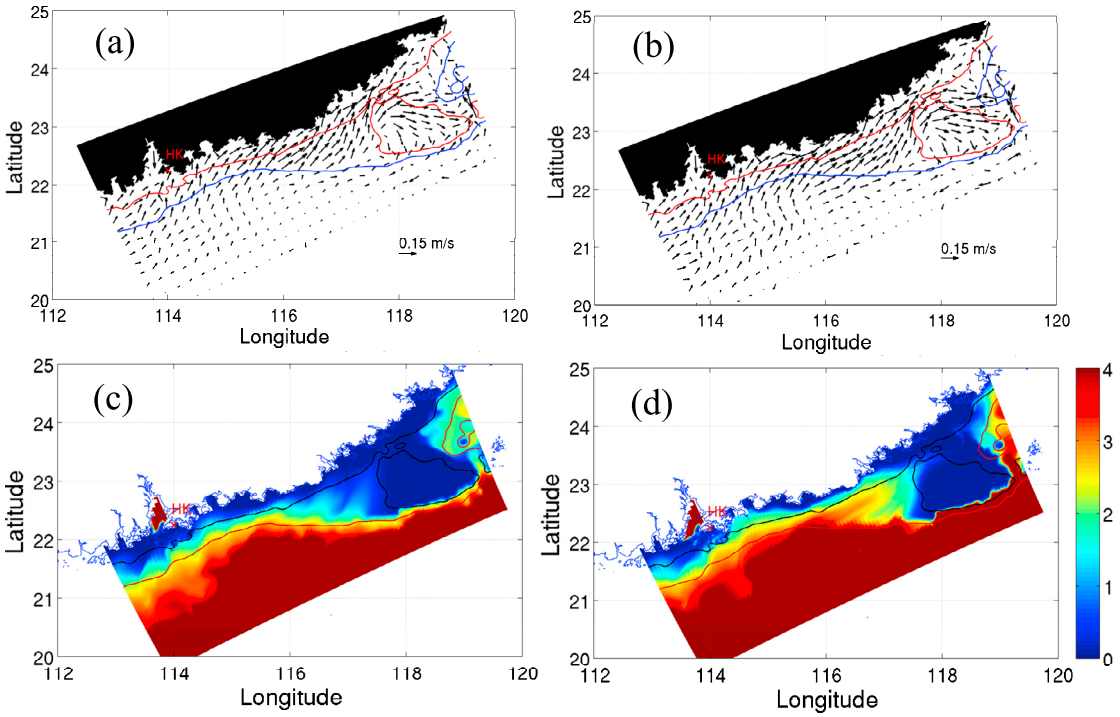

Figure 8. Bottom (a and b) velocity vectors (m s^{-1}) and (c and d) NO_3 (mmol m^{-3}) on days 10 (left) and 30 (right).

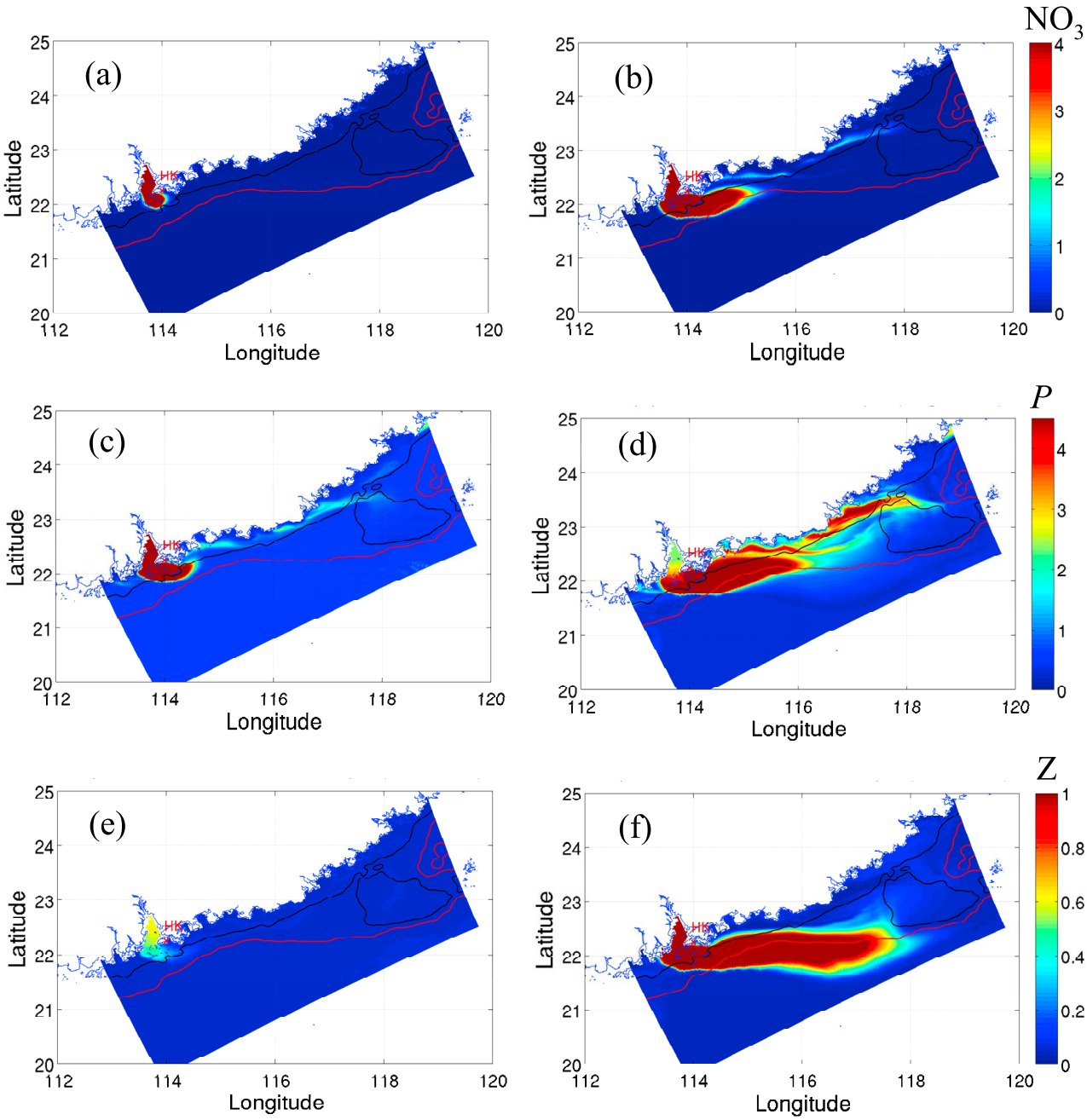

Figure 9. Surface (a and b) NO_3 (mmol m^{-3}), (c and d) chlorophyll (mg m^{-3}), and (e and f) zooplankton (mmol m^{-3}) on days 10 (left) and 30 (right).

as also shown by the field measurements (Figure 3). Blooms of phytoplankton (shown as chlorophyll) in both initial and mature stages are correlated with the nitrate distribution, but have larger alongshore and offshore extensions. Because of the time lag between phytoplankton and zooplankton, there is no obvious growth of surface zooplankton over the shelf on day 10, except in the surface water outside the estuary. On day 30, a relatively high zooplankton concentration occurs in the intensified upwelling zone in the lee of the coastal cape off Shantou. However, a much higher Z concentration exists in the plume, which is clearly one of the major contributors to biomass in the NSCS. Through monthly dilution experiments at a station in the plume and a station mostly affected by the SCS seawater in the region, M. Chen et al. (Temporal variations of mesozooplankton assemblage and grazing activity in estuarine and coastal waters of Hong Kong: The effects of temporal stratification, submitted to *Journal of Plankton Research*, 2009) recently found that Chl-*a*, microzooplankton biomass, phytoplankton growth and microzooplankton grazing rates were higher in the plume station than in the coastal station.

4.2. Vertical Structure of the Ecosystem

[21] To illustrate the variable three-dimensional responses of the ecosystem to coastal upwelling and the river plume, physical and biological variables in the across-shelf

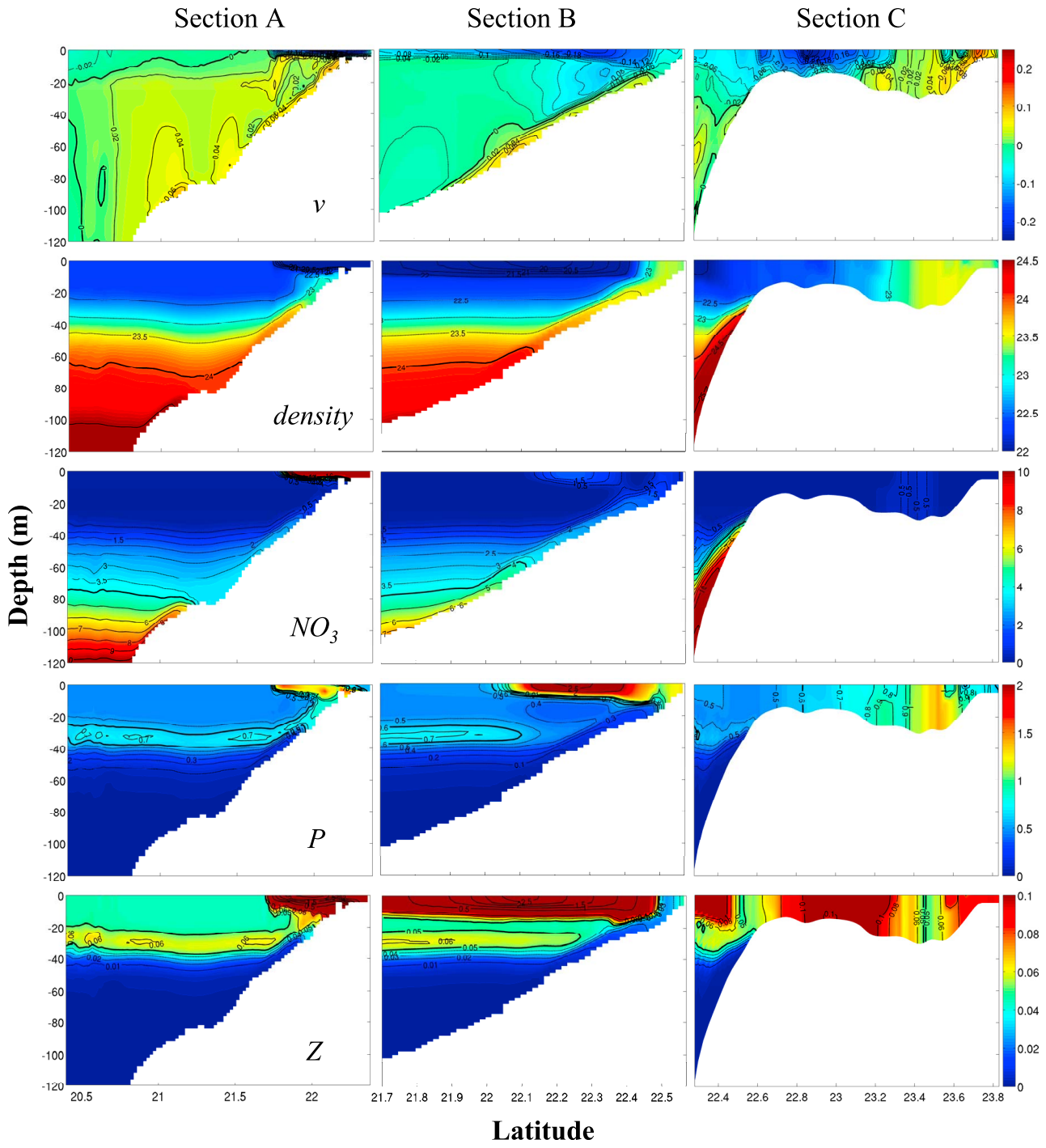

Figure 10. Across-shore sections of cross-shelf velocity v (m s^{-1}), salinity (psu), NO_3 (mmol m^{-3}), phytoplankton (P, mmol m^{-3}), and zooplankton (Z, mmol m^{-3}) at (left) lines A, (middle) B, and (right) C on day 30.

sections A at the PRE, B near Shanwei, and C at the Taiwan Shoals (Figure 1) are presented for day 30 in Figure 10.

[22] In sections A and B, the seaward currents in the upper Ekman layer advect the nutrient-rich waters offshore in the upwelled zone and in the plume. The shoreward velocities and thus the shoreward transport of dense and nutrient-rich deep water are mainly found in the bottom frictional boundary layer with much stronger intensities in section B. The up-slope transport of nutrient-rich dense deep water occurs underneath the buoyant river plume during upwelling.

[23] Quite different conditions exist in section C. The nutrient-rich dense water shoreward of the Taiwan Shoals that did not originate from offshore, but apparently was advected from upstream (west). The up-slope nutrient advection occurs seaside of the Taiwan Shoals but is limited only to the offshore side of the shoals without reaching the inner shelf. Although shoreward currents also exist in the interior of the

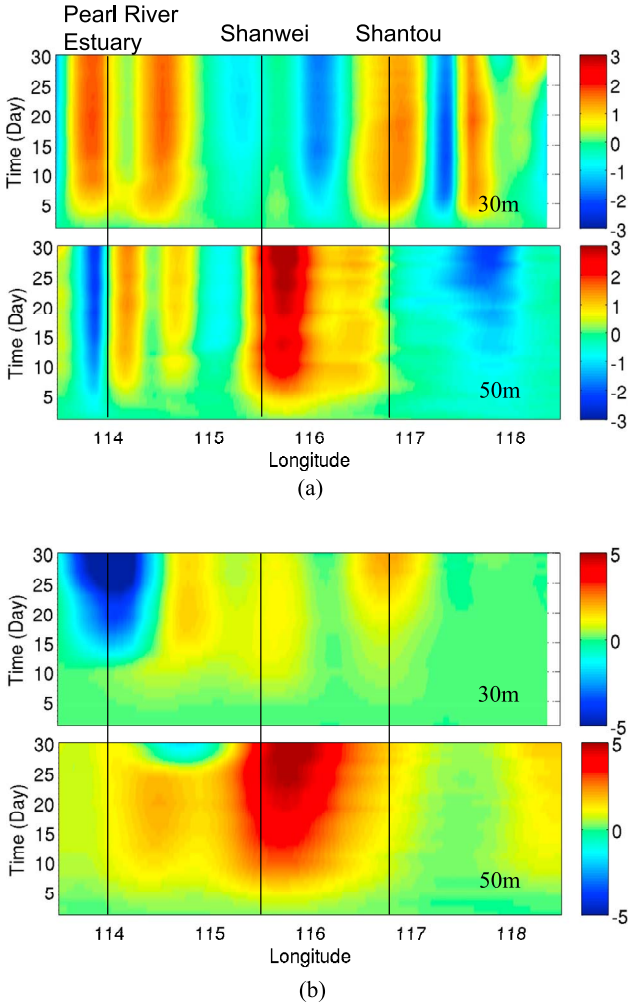

Figure 11. Time series of depth-integrated (a) volume flux (m^2 s^{-1}) and (b) nitrate flux (mmol m^{-1} s^{-1}) across the 30 m and 50 m isobaths during upwelling. The positive/negative fluxes direct shoreward/seaward, respectively.

water column along A and B sections, their ability to transport nutrients shoreward is very limited because of the weak horizontal gradient of N in the interior.

[24] In sections A and B, the phytoplankton blooms in the near-shore upwelled waters and the offshore plume are separated by newly upwelled water with a relatively low concentration of phytoplankton. As a combined result of offshore surface Ekman transport and the lag response in phytoplankton growth after the nutrient uptake, the phytoplankton bloom tends to be located farther offshore than the nutrient-rich upwelled water in the surface along these two sections. In section C, the phytoplankton bloom is not visible seaward of the bank; the bloom on the shore side grows first from the bottom layer and then gradually extends to the entire water column. Unlike those in sections A and B, the bloom in section C occurs in the water closer to shore compared to the location of the nitrate presumably due to weaker offshore currents.

[25] In general, the zooplankton distribution has the largest cross-shelf extension. This reflects the combined effects of the cross-shelf circulation and the different response times of the ecosystem. A SCM was formed at 30–40 m (Figure 10) in sections A and B and in the offshore waters in C. The SCM is elevated in the nearshore waters in section A but disappears under the plume in section B as also shown by [*Lu et al.*, 2010]. Overall, vertical features in the simulated Chl-*a* and N agree reasonably well with those in the observations (Figure 5).

5. Analyses and Discussion

5.1. Cross-Isobath Nutrient Transport

[26] Wind-driven upwelling circulation transports nutrient-rich deep water to the euphotic zone for utilization by a potential algal bloom. The shoreward nutrient transport during upwelling is shown in the time series of depth-integrated (Figure 11) and depth-dependent (Figure 12) cross-isobath volume and nutrient fluxes along the 30 and 50 m isobaths on day 30. The respective cross-isobath volume (M_y) and nutrient (N_y) fluxes are obtained by

$$M_y = \int_{h_1}^{h_2} (v_0 \cos\theta - u_0 \sin\theta) dz, \tag{8}$$

and

$$N_y = \int_{h_1}^{h_2} (v_0 \cos\theta - u_0 \sin\theta) NO_3 dz, \tag{9}$$

where (u_0, v_0) are the eastward and northward currents, respectively, and θ is the angle between the tangent direction to the isobath and true east. h_1 and h_2 are the depths at the top and bottom of the integrated layers, respectively. The subscript y refers to the direction normal to the isobath.

[27] Within the first 3 days after the onset of southwesterly winds, the spatially variable cross-isobath mass flux (M_y) becomes apparent over the inner and middle shelves. Although M_y in the water column along both the 30 and 50 m isobaths has alternating shoreward and seaward flux (Figure 11a), net N_y is always shoreward (positive) except near the PRE where the plume water with high nitrate flows seaward. The magnitudes of M_y and N_y transports increase with time as upwelling develops. The strongest N_y occurs along the 50 m isobath over the middle shelf at the head of the widened shelf (near Shanwei), where enhanced bottom Ekman transport and shoreward geostrophic currents advect nutrient-rich, deep water toward the inner shelf over the steep midshelf. These strongest shoreward M_y and N_y over the middle shelf, however, do not reach the inner shelf near Shanwei; instead, they appear farther downstream near Shantou, similar to the response in the temperature field. The results indicate that most of the shoreward flux from the middle shelf is advected downstream by alongshore upwelling flow as it is approaching the inner shelf. In addition to the prominent along-isobath variation of cross-isobath flux around the widened shelf, other alternating shoreward/seaward transports exist along the coast which are induced either by the buoyancy in the spatially variable Pearl River plume or by the concave/convex variation of the coastline [*Gan et al.*, 2009a].

[28] N_y, does not always flow in the same direction as M_y (Figure 11b). The diversion is caused by the depth-dependent nitrate concentration and variable cross-isobath velocity in

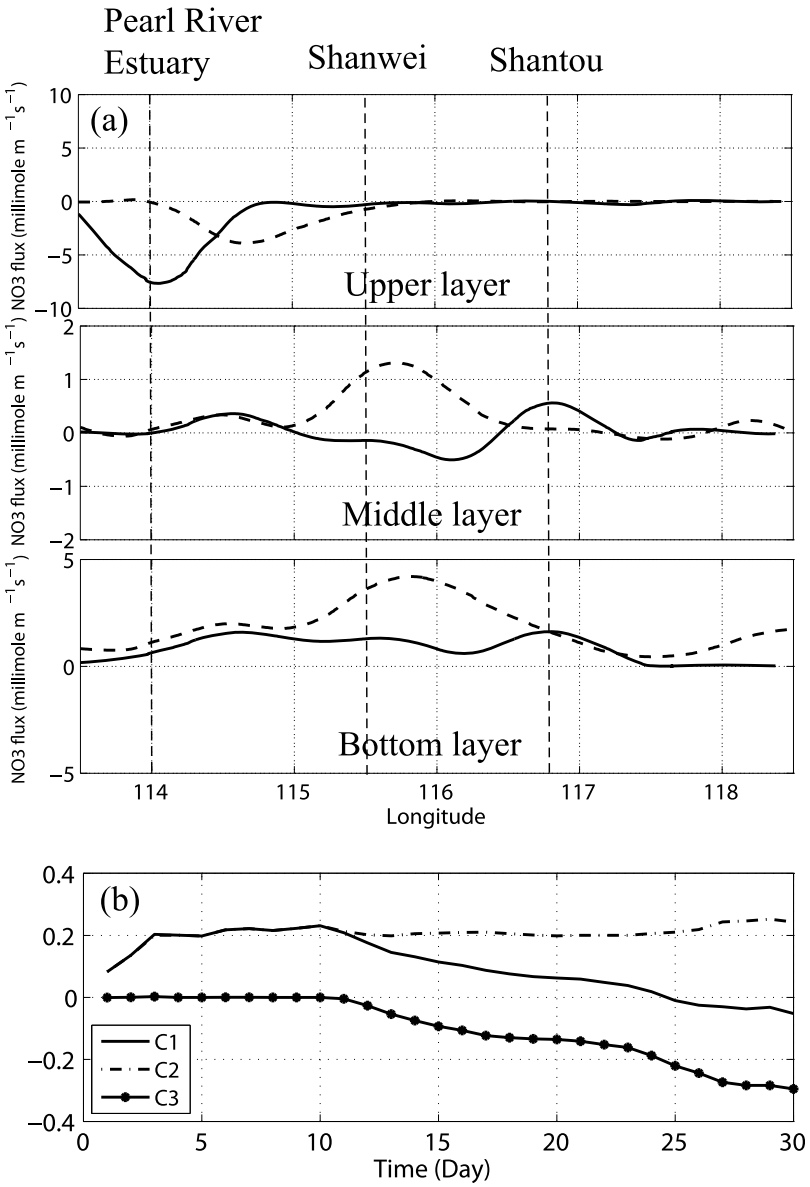

Figure 12. (a) Daily averaged N_y flux (millimole m^{-1} s^{-1}) normal to the 30 m isobath (solid line) and the 50 m isobath (dashed line) on day 30. They are depth-integrated for the upper 10 m (upper layer); middle 10 m at a depth of 30 m, 30 m at a depth 50 m (middle layer); and for the bottom 10 m (bottom layer). Positive values of transport are directed shoreward. (b) Time series of ratios of depth-integrated cross-isobath N transport along the 30 m isobath ($\overline{N}_{y30m}$) to the corresponding transport along the 50 m isobath $\overline{N}_{y50m}$ (line C1); the shoreward transport along the 30 m isobath $\overline{N}_{y30m} > 0$ to $\overline{N}_{y50m}$ (line C2) and their difference C3 = C1−C2. The values of transport are averaged between 114.5°E and 118.5°E.

the water column. Figure 12a shows that the enhancement of offshore Ekman transport over the nutrient-rich river plume forms a seaward N_y flux in the upper layer near the entrance of the PRE and at the location farther east over the mid-shelf, despite the mainly positive M_y in the water column (Figure 11a). A positive N_y primarily occurs in the bottom boundary layer of the inner and middle shelves due to Ekman transport and partly in the middle layer of the middle shelf due to geostrophic shoreward current (Figure 12a). Thus, the cross-shelf nutrient transport in the NSCS during upwelling is distinctly controlled by seaward transport in the plume layer and shoreward transport in the bottom frictional layer.

[29] To investigate the efficiency of the cross-shelf nutrient transport in the NSCS, a time series of the ratio of cross-isobath N transport $\overline{N}_{y30m}$ over the inner shelf (depth-integrated and averaged along the 30 m isobath) to the corresponding transport $\overline{N}_{y50m}$ over the middle shelf, or $\overline{N}_{y30m}/\overline{N}_{y50m}$ (line C1), the ratio of positive (shoreward) $\overline{N}_{y30m} > 0$ to $\overline{N}_{y50m}$, or $\overline{N}_{y30m} > 0/\overline{N}_{y50m}$ (C2), and their difference C3 = C1−C2 are shown in Figure 12b. Line C1 illustrates the relative magnitude of net nutrient transport between the inner and middle shelves. Line C2 is the percentage of nutrient contribution by the upwelling that crosses the middle shelf and reaches the euphotic layer over the inner shelf. The result of

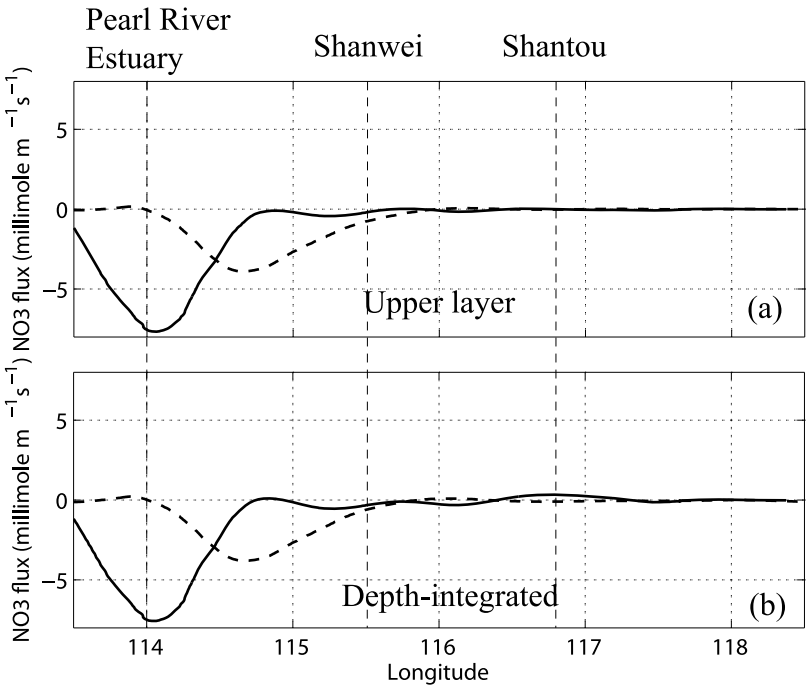

Figure 13. The differences of nitrate flux normal to the 30 m isobath (solid line) and the 50 m isobath (dashed line) between the cases with and without river discharge (a) in the upper layer and (b) over the entire water column on day 30.

C1 indicates that about 20% of the total shoreward nutrient flux from the middle shelf reaches the inner shelf by day 10 before the plume arrives. Afterwards, an increasing seaward *N* transport in the river plume gradually decreases the shoreward *N* transport over the shelf and eventually, the net cross-shelf *N* transport in the NSCS becomes seaward by day 25. By limiting $\overline{N}_{y30m}$ to be positive, or by excluding the offshore transport contributed by the river plume, C2 shows that 20% of shoreward and upward *N* transport from the middle shelf steadily reaches the inner shelf during upwelling. The increasing offshore *N* transport in the plume (C3) eventually offsets the nutrient imported by wind-driven upwelling in the NSCS. We found that the offshore *N* transport by the plume is delayed by about 10 days if the river discharge rate or *N* concentration in the river is reduced by 50%.

[30] To understand the role of the river discharge in the cross-shelf *N* transport, the differences of nitrate flux normal to the 30 m (solid line) and the 50 m isobath (dashed line) between the cases with and without river discharge are shown in Figure 13a. The case without river discharge is implemented in the same way as the standard case, but without river discharge. By comparison with the result in Figure 12a for the standard case, it is found that the difference of the transport across the inner and middle shelves in the upper layer west of Shanwei is totally contributed by the plume. The difference contributed by upwelling, mainly to the east of Shanwei, is very small. Since the difference in depth-integrated field (Figure 13b) is identical to that in the upper layer (Figure 13a), it suggests that the plume has little effect on the transport in the nonplume deeper layer. The offshore nutrient transport in the plume gradually decreases from the inner shelf to the middle shelf and from the source region to the far field of the plume as it propagates seaward and eastward.

5.2. Spatial Disparity of *N*, *P*, and *Z*

[31] The phytoplankton blooms in the plume have larger alongshore and offshore excursions than the concomitant field of *N*. Subsequently, the zooplankton distribution has even larger alongshore and offshore excursions than the chlorophyll field. The evolution of the eastward propagation of the surface velocity, salinity, and biological variables in the plume is seen in the time series along the plume axis at 22.1°N (Figures 14a and 14b). The plume is first formed as a quasi-stationary freshwater bulge containing a high concentration of *N* after leaving the estuary as shown by the time series in Figure 14b. As the bulge grows, its outer part gradually accelerates eastward at about 0.07 m s^{-1} west of 114.5°E. During this process, the high concentration of *N* in the plume is limited in the region west of 115°N and is exhausted by the uptake of *P* farther east. Although *N* is abundant within the bulge, strong grazing pressure substantially lowers the *P* concentration after Z reaches its relatively high concentration by day 20. Away of the bulge, the plume moves at the current speed of about 0.2 m s^{-1}. In the far field, the downstream advected *P* quickly decreases, particularly in the region east of 115°N after day 20 when *Z* concentration becomes significant. The result is the spatial disparity of *N*, *P*, and *Z* as shown in Figure 14a. Although field measurements of *Z* are not available, field measurement (Figure 3) shows the similar spatial variation among salinity, *N* and *P* in the plume. Unlike *N* and *P*, the downstream-advected high concentration of *Z* in the plume is transported farther east with a pattern similar to that of salinity. The different growth rates among variables in the compartments of Figure 6 are also responsible for the spatial dislocations of *N* and *P* and for the broad spatial extension of *Z* in addition to the concomitant effects of alongshore and cross-shore currents. By the same argument, a

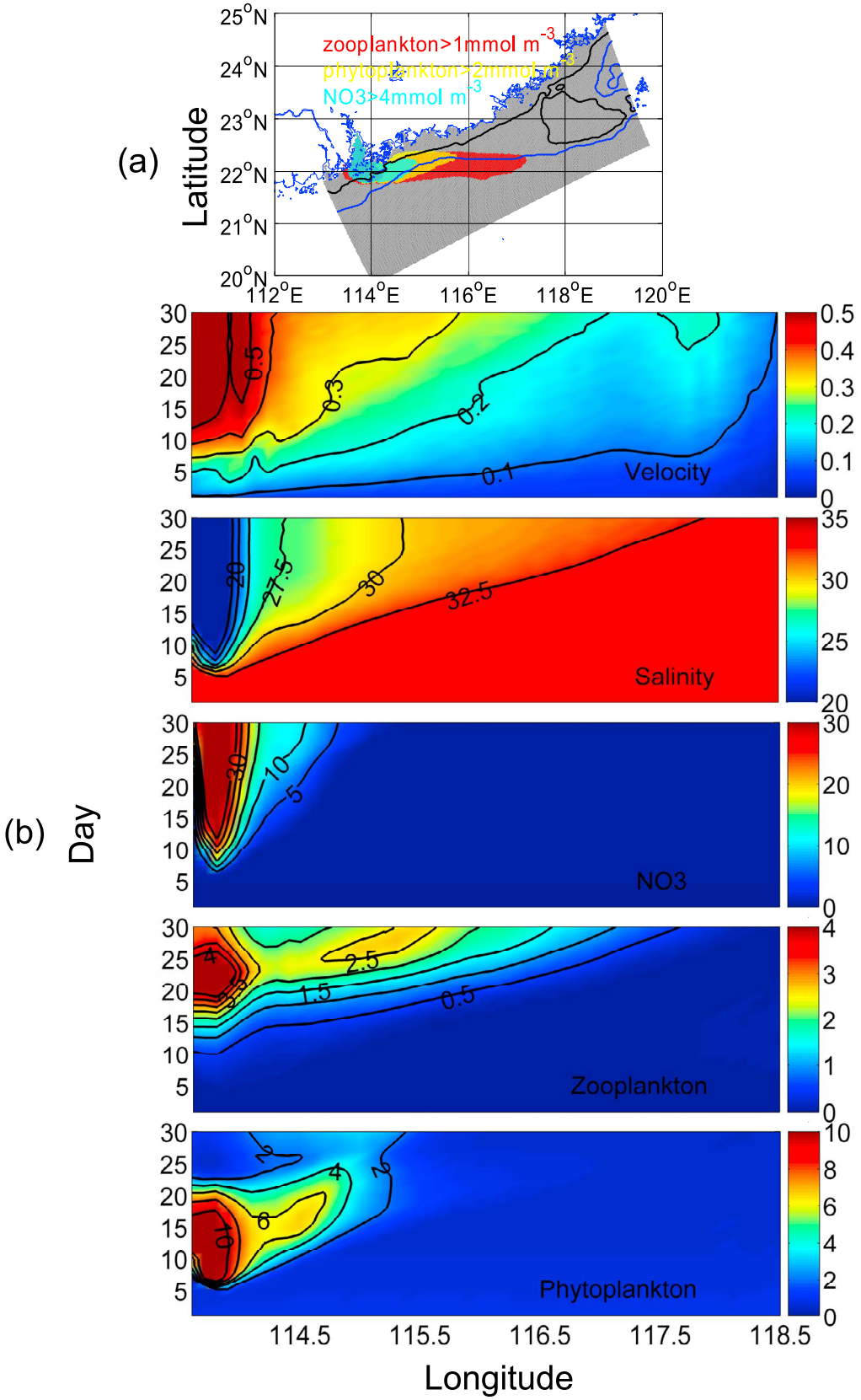

Figure 14. (a) Surface NO_3, phytoplankton, and zooplankton (mmol m^{-3}) greater than their respective thresholds in the plume on day 30, and (b) time series of along-plume velocity (m s^{-1}), NO_3, phytoplankton, and zooplankton (mmol m^{-3}) as a function of distance along the axis of the plume (22.1°N).

similar dislocation of P and Z also occurs in the offshore direction due to both physical and biological forcing as shown in Figure 14 (also see Figures 9 and 10).

[32] To better illustrate the process, the result from the case without the inclusion of the river discharge is also presented. With a steady northeastward wind stress (τ) of 0.025 Pa, we estimate the seaward surface Ekman velocity as $v_{ey} = \frac{\tau}{\rho_0\sqrt{A_z f}}\sin\frac{\pi}{4}$, where ρ_0 is the water density and f is the Coriolis parameter. With the vertical eddy viscosity coefficient, A_z, derived from the embedded turbulent model along line B on day 30, v_{ey} is about 0.04 m s^{-1} in the upwelling zone and about 0.08 m s^{-1} in the plume. Thus, the time lag to form the average offshore dislocations of ~10 km in the upwelling zone and ~20 km in the plume, between P and Z (Figure 15), is about 3 days, less than the 6–9 days calculated by *Spitz et al.* [2005]. The P-Z disparity stays relatively constant during upwelling, suggesting that the biological processes (e.g., grazing of P, uptake of N, and mortality), are consistently occurring during the course of offshore movements in P and Z and that a dynamic balance is achieved between plankton growth and Ekman transport. In the nutrient-rich upwelling zone and plume, phytoplankton first grows from very low concentrations followed by growth of zooplankton after phytoplankton reach a certain concentration. The rapid increase in phytoplankton depletes N quickly and the grazing pressure by zooplankton then subsequently decreases the phytoplankton biomass. Both biological forcing and the surface Ekman forcing characterize biological responses in the NSCS which is similar to the finding of *Baird et al.* [2007] and *Spitz et al.* [2005]. It is worth noting that the relatively low biomass of phytoplankton and zooplankton from the newly upwelled water dilutes the surface plankton when the plume is absent (Figure 15b).

5.3. Evolution of Ecosystem

[33] Besides the physical forcing, the variation in nutrients and thus the ecosystem is also controlled by the underlying biogeochemical processes in the euphotic zone. First, we focus on the responses in the upwelled water. Upwelled water is defined as the water with a salinity >33.75 in the upper 20 m, within which PAR decreases to about 10% of the surface value and where the major biological productivity occurs (Figures 7 and 10). The time series of N, P, Z, A, and D, averaged in the upwelled water (Figure 16), are calculated by

$$(N,P,Z,A,D) = \frac{1}{V}\int_V (N,P,Z,A,D)dV, \qquad (10)$$

where V is the volume of the upwelled water. Figure 16 shows that the nutrient-rich upwelled water becomes apparent around day 10 and increases continuously. N starts to decrease around day 20 while the biomass of phytoplankton reaches its maximum around day 32. Time lags between wind stress and the response of N, P, and Z. have been reported by others, for example, roughly 3–4 days between P and N and 13–16 days between Z and wind stress on the Oregon shelf [*Spitz et al.*, 2005], and lags of 6–10 days between P and wind stress along the California coast have been previously reported [*Dugdale and Wilkerson*,1989; *Service et al.*, 1998]. In the case when N is supplied by upwelling, phytoplankton grows by taking up N. The growth slows when N is depleted. The continuous increase in grazing pressure causes phytoplankton to decrease after it has reached its maximum. This produces a time lag between phytoplankton and Z. Generally, the phytoplankton concentration is below the half-saturation concentration of phytoplankton ingestion, so the biomass of Z keeps increasing with a relatively lower growth rate.

[34] The evolution of the biological response within the plume water (with salinity < 33 over the shelf) is shown by the time series of plume-averaged biological variables in Figure 17. Because of the high turbidity and possible phosphorus limitation in the estuary [*Zhang et al.*, 1999; *Yin et al.*, 2000; *Xu et al.*, 2008], the water mass in the PRE is excluded from the time series. After exiting the estuary, the plume gradually expands eastward and N within the plume increases over the shelf in the first 12 days. However, the average N in the plume decreases due to the biological uptake and dilution by the nutrient-poor ambient seawater during its offshore expansion from the PRE. Phytoplankton reach their maximum concentration around day 10, decrease quickly, and attain an equilibrium around day 27. This time-dependent response in phytoplankton is likely associated with the rapid expansion of the river plume and the high grazing pressure from zooplankton at the initial stage, and then by the subsequent balance between the growth of phytoplankton and the grazing from zooplankton when the volume of the plume becomes relatively stable. Here, N is not confining the growth of phytoplankton since its concentration is always higher than the half-saturation concentration that is needed for phytoplankton uptake. As a result of the high phytoplankton concentration (higher than the half-saturation concentration of phytoplankton ingestion) before attaining equilibrium, the biomass of zooplankton increases due to their high growth rate and reaches a maximum concentration on day 26. Afterward, the zooplankton concentration becomes relatively stable due to the confinement of the phytoplankton.

5.4. Biological Contrasting in the Plume and Upwelling

[35] The relative importance of upwelling and the plume to biological productivity over the shelf is shown by the time series of ratios of volume-integrated (N, P, Z, A) in the plume to those in both plume and upwelled water (Figure 18). P concentration in the plume is initially higher but becomes comparable with that in the upwelled water after day 25 when the ecosystem in the plume has stabilized. The total biomass is mainly due to input by the plume in the NSCS. After day 10 when the plume reaches the shelf at about 114.5°E, the percentage of the N concentration in the plume over the shelf decreases from 85 to ~70% within the first 20 days. A much slower decrease in the ratio of N occurs after day 20 due to the phase lag of N in upwelled and plume waters as shown in Figures 16 and 17. The ratio of P in the plume decreases from 95 to ~55% from day 10 to 30 because of the increase of grazing, but it becomes constant afterward. The plume water steadily contributes more than 95% of the total Z in the NSCS during the upwelling season, suggesting a consistent pattern of Z variation in both upwelled and plume waters. The plume contributes about 70% of the total inorganic nitrogen, 65% of phytoplankton biomass, and 95% of zooplankton biomass in the shelf waters at the time when river discharge is strong in upwelling season. The zooplankton to phytoplankton ratio is relatively small and stable in the upwelled waters as compared with that in the plume. A larger contribution of biomass

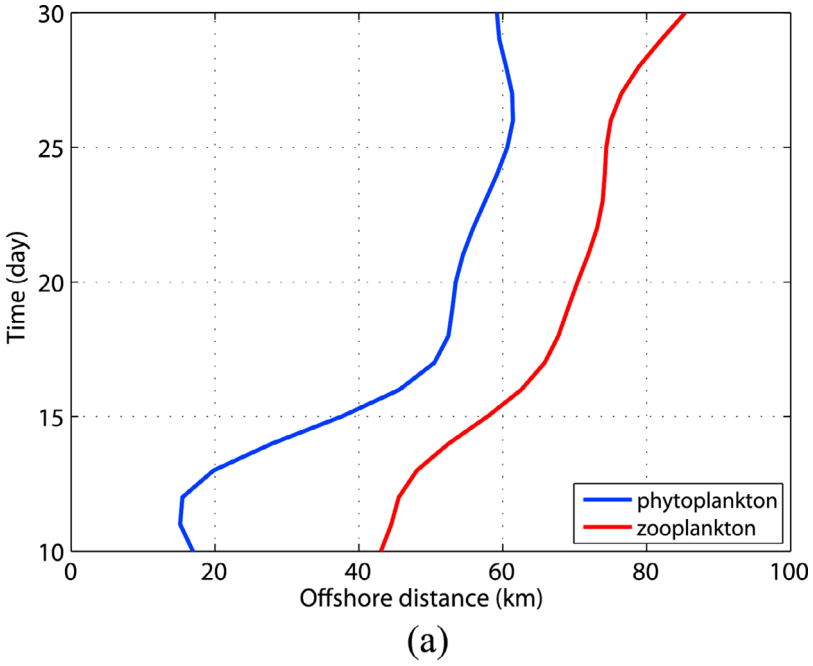

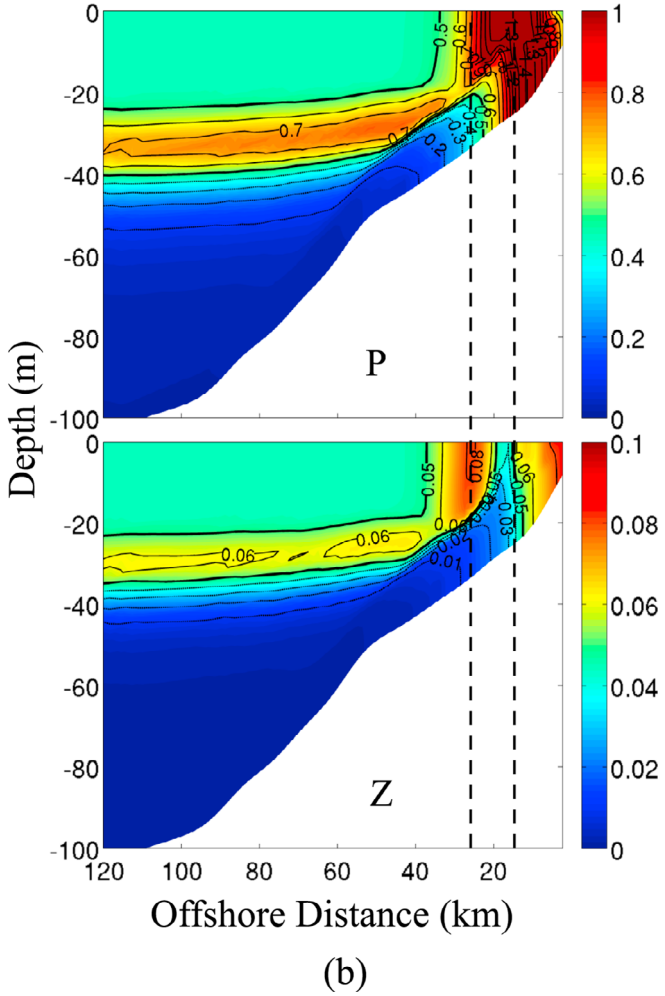

Figure 15. (a) Offshore distance of the maximum concentrations of surface phytoplankton and zooplankton (mmol m^{-3}) at line B for the case with river plume and (b) across-shore section of phytoplankton (P) and zooplankton (Z) (mmol m^{-3}) at line 305 for the case without river on day 30.

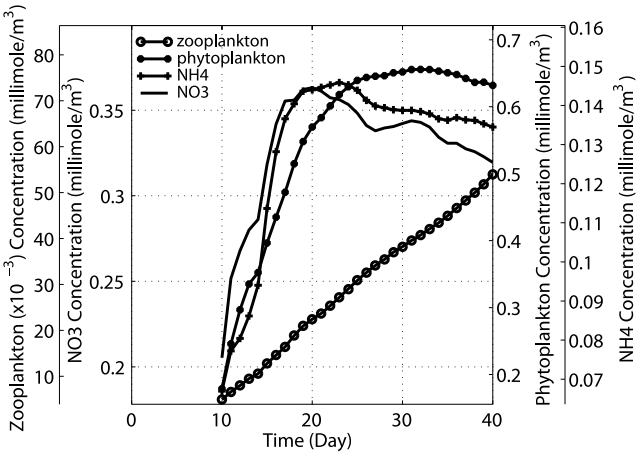

Figure 16. Time series of NO_3, phytoplankton, zooplankton, and NH_4 (mmol m^{-3}) in the wind-driven upwelled waters over NSCS.

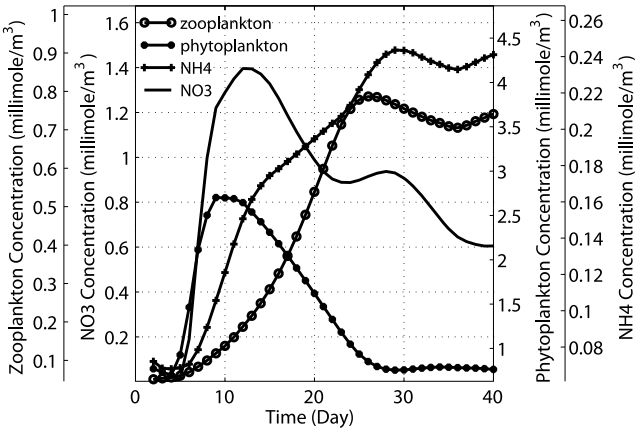

Figure 17. Time series of NO_3, phytoplankton, zooplankton, and NH_4 concentrations (mmol m^{-3}) in the plume.

in the plume is probably caused by the stronger biological productivity in the warmer plume. The differences in temperature, light attenuation [*Lu et al.*, 2010], and nutrient concentration between the upwelled and plume waters produce the different growth rates of phytoplankton (Figure 19).

[36] The respective contributions in the plume and in the upwelled waters to depth-integrated primary production (IPP) are shown in Figure 20. The plume and upwelled waters are defined in section 5.3 and the IPP excludes the primary production outside of the plume and upwelled waters, such as in the SCM layer. A larger contribution is always found in the plume, although the difference in IPP between the plume and upwelled waters becomes smaller when the biological system reaches a mature stage on about day 30. Interestingly, a smaller growth rate (Figure 19) in the plume before day 20 has a larger IPP, but IPP quickly decreases toward the mature stage despite the continuous increase in growth rate. Besides the physical processes involving in the wind-driven shelf circulation, grazing (Figure 19) and other biological forcing (Figures 16 and 17) jointly control the course of the biological development in the plume. In the upwelled waters, IPP monotonically increases toward the mature stage with a relatively stable growth rate.

6. Summary

[37] The ecosystem responses to the distinctly intensified coastal upwelling over the widened shelf and to the Pearl River plume in the NSCS have been examined with observations and a three-dimensional coupled physical-NPZD ecosystem model. The objective was to examine the biological responses to the upwelling in the NSCS with highly variable shelf topography, the estuary and bays along the coastline, and a sizable river discharge. With analyses of observational evidence and successful simulation of the observed ecosystem characteristics in the NSCS, this study investigated the processes involving nutrient enrichment by the coastal upwelling and by a river plume. It also identified subsequent ecosystem dynamics that are jointly controlled by physical and biological forcing.

[38] During the upwelling wet season, two highly productive centers coexist over the shelf in the NSCS because of nutrient enrichment by the intensified upwelling and by the river plume. Driven by the southwesterly wind stress during summer, the coastal circulation in the NSCS is characterized by the intensified upwelling over a widened shelf. A strong, up-slope, nutrient-rich flux crosses the steep middle shelf at the head of the widened shelf. Developing coastal currents then move the up-sloping nutrient-rich waters farther downstream, which subsequently outcrops at the lee of a coastal cape. This physically forced nutrient enrichment forms a distinctive highly productive region over the widened shelf. The ecosystem in the upwelled water matures in 20 days after the onset of the upwelling-favorable winds and the nitrate concentration starts to decline due to phytoplankton uptake. During the upwelling, about 20% of the nutrient that crosses the middle shelf from deep water reaches the inner shelf and fuels a potential phytoplankton bloom.

[39] The motion of the plume in the NSCS is largely controlled by upwelling circulation over the shelf after the plume exits the PRE. At the same time, the buoyancy of the plume also greatly modulates the wind-driven surface flow. The nutrient-rich plume water forms a bulge at the entrance of the PRE, but then it spreads over the shelf east of the PRE due to

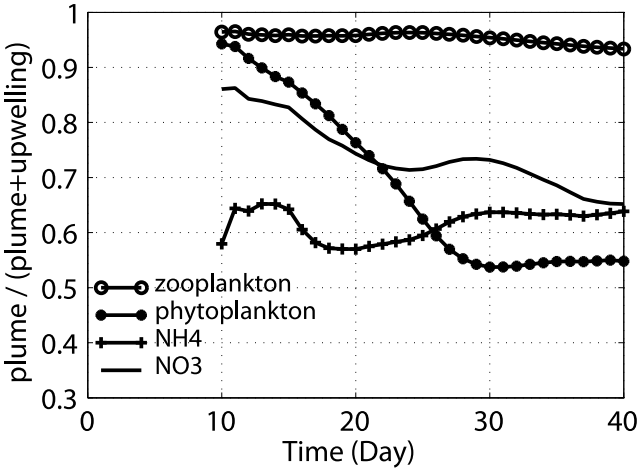

Figure 18. Time series of ratio of volume-integrated NO_3, phytoplankton, zooplankton, and NH_4 in the plume to the total concentrations in the plume plus in the upwelled waters.

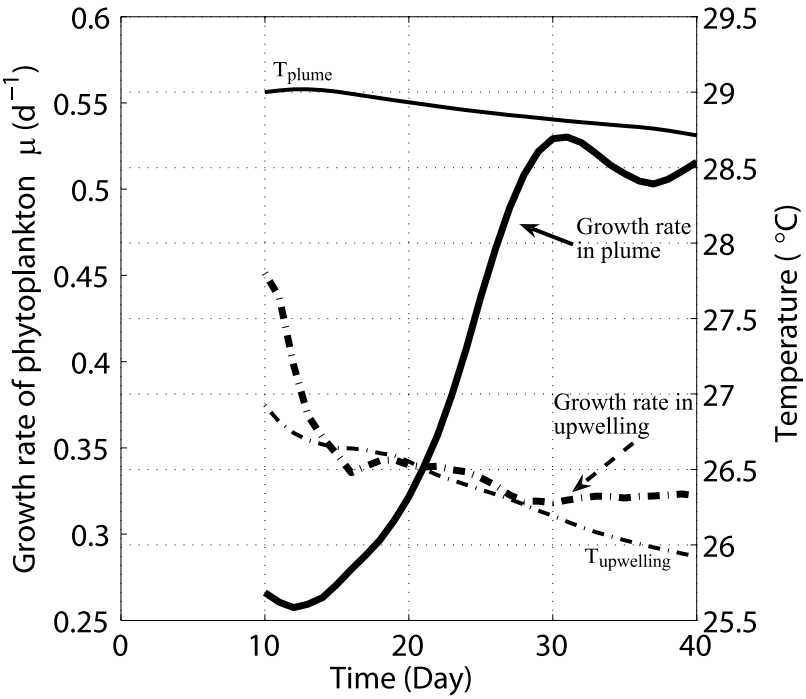

Figure 19. Time series of temperature (°C) and growth rates (d^{-1}) averaged in the plume and in the upwelled waters, respectively.

upwelling circulation. With increased efficiency in the surface Ekman layer within the plume layer, the algal bloom in the plume expands seaward as it propagates eastward. In the wet season, with a discharge rate of ~16,000 m^3 s^{-1}, the nutrients in the plume contribute about 70% of total nutrient load and 80% of total biomass to the shelf waters. Biological productivity is higher in the plume than that in the upwelled water.

[40] Biogeochemical responses in both the upwelled and plume waters exhibit strong temporal and spatial variations among *N*, *P*, and *Z*. Typically, *N* reaches its peak value before *P*, and the maximum *Z* bloom occurs after the peak *P* bloom. This is controlled by the upwelling circulation and by the different growth rates and growth time lag in *P* and *Z*. Zooplankton are generally located farther offshore than the phytoplankton as a result of Ekman drift and the time lag between the response of phytoplankton and zooplankton. Jointly controlled by the biological and physical forcing in the plume, *N*, *P*, and *Z* abundance has a distinct along-plume distribution in which *Z* and *N* have the largest and the smallest eastward and seaward extensions, respectively. This study has demonstrated the importance of physically controlled biological responses in the intensified upwelling and plume-influenced NSCS shelf.

Appendix A

[41] *The variable* μ is the growth rate of phytoplankton:

$$\mu = \mu_{\max} * f(I) * \left(\frac{[N]}{k_N + [N]} * \frac{1}{1 + [A]/k_A} + \frac{[A]}{k_A + [A]} \right) \quad \text{(A1)}$$

$$\mu_{\max}(T) = \mu_0 \cdot 1.066^T, \quad \text{(A2)}$$

where $\mu_{\max}$ is the maximum growth rate of phytoplankton, *N* is nitrate, K_N is the half-saturation constant for phytoplankton uptake by NO_3, *A* is ammonium, K_A is the half-saturation constant for phytoplankton NH_4 uptake by phytoplankton, and *T* is temperature. The phytoplankton growth rate μ_0 is

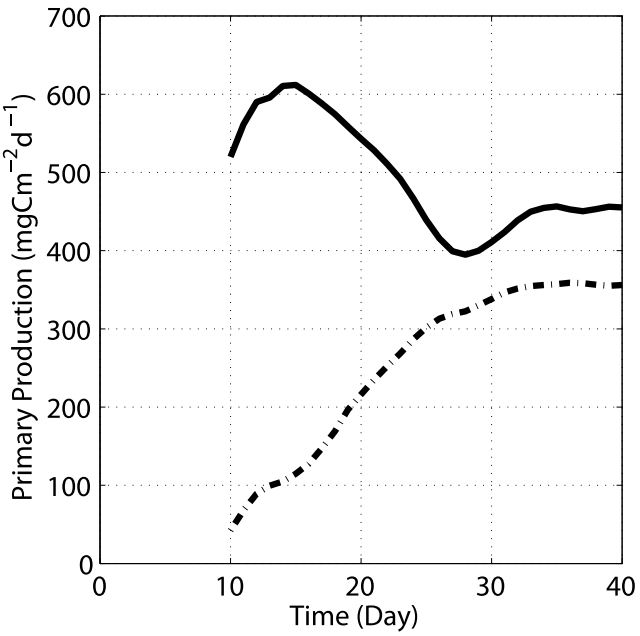

Figure 20. Time series of primary production within the plume (solid line) and within the upwelled (dashed line) waters, respectively.

$0.59\ d^{-1}$. The function $f(I)$ represents the photosynthesis-light (P-I) relationship [*Evans and Parslow*, 1985],

$$f(I) = \frac{\alpha I}{\sqrt{\mu_{\max}^2 + \alpha^2 I^2}} \tag{A3}$$

$$I = I(z) = I_0 * par * \exp\left\{ -z * \left(K_w + K_{chl} * \int_z^0 Ch(\varsigma) d\varsigma \right) \right\}, \tag{A4}$$

where I is the same as PAR, I_0 is the incoming light just below the sea surface, α is the initial slope of the P-I curve, par is the fraction of light that is available for photosynthesis and equals 0.43, K_w is the light attenuation coefficient for seawater, and K_{chl} is the light attenuation coefficient for chlorophyll.

[42] **Acknowledgments.** This research was supported by the National Key Basic Research Development Program 2009CB421208, by Hong Kong's Research Grants Council and the National Natural Science foundation of China under grants NSFC-RGC project (N_HKUST623/07 and NSFC 40731160624), by Hong Kong's Research Grants Council CERG-601008, and by the SCOPE project co-organized by Jiang Zhu, Dongxiao Wang, Xiaogang Guo, Minhan Dai, and Jianping Gan. Field work was assisted by Jianyu Hu and Bangqin Huang and is highly appreciated. The authors are grateful to the helpful suggestions provided by Peter Franks. We thank two anonymous reviewers for helpful comments.

References

Baird, M. E., O. Leth, and J. F. Middleton (2007), Biological response to circulation driven by mean summertime winds off central Chile: A numerical model study, *J. Geophys. Res.*, *112*(C7), C07031, doi:10.1029/2006JC003655.

Boyer, T., S. Levitus, H. Garcia, R. A. Locarnini, C. Stephens, and J. Antonov (2005), Objective analyses of annual, seasonal, and monthly temperature and salinity for the world ocean on a 0.25 degrees grid, *Int. J. Climatol.*, *25*(7), 931–945.

Cai, Y., X. Ning, and C. Liu (2002), Distribution characteristics of size-fractionated chlorophyll a and productivity of phytoplankton in the Northern South China Sea and Beibu Gulf during August 1999 (in Chinese), *Stud. Mar. Sinica*, *44*, 11–21.

Chen, Y. L. L., H. Y. Chen, D. M. Karl, and M. Takahashi (2004), Nitrogen modulates phytoplankton growth in spring in the South China Sea, *Cont. Shelf. Res.*, *24*(4–5), 527–541.

Dai, M. H., et al. (2008), Effects of an estuarine plume-associated bloom on the carbonate system in the lower reaches of the Pearl River estuary and the coastal zone of the northern South China Sea, *Cont. Shelf Res.*, *28*(12), 1416–1423.

Du, F. Y., C. H. Li, X. L. Liao, X. P. Jia, and X. H. Wang (2006), The variety of zooplankton biomass in Daya Bay (in Chinese), *Mar. Environ. Sci.*, *25*, 37–43.

Dugdale, R. C., and F. P. Wilkerson (1989), New production in the upwelling center at Point Conception, California: Temporal and spatial patterns, *Deep Sea Res., Part A*, *36*, 985–1007.

Evans, G. T., and J. S. Parslow (1985), A model of annual plankton cycles, *Biol. Oceanogr.*, *3*, 327–347.

Evans, G. T., and V. C. Garcon (Eds.) (1997), One-dimensional models of water column biogeochemistry: Report of a workshop held in Toulouse, France, November–December 1995, *JGOFS Rep.*, *23*, 85 pp., Joint Global Ocean Flux Study, Bergen, Norway.

Fasham, M. J. R., H. W. Ducklow, and S. M. McKelvie (1990), A nitrogen-based model of plankton dynamics in the oceanic mixed layer, *J. Mar. Res.*, *48*, 591–639.

Fennel, K., J. Wilkin, J. Levin, J. Moisan, J. O'Reilly, and D. Haidvogel (2006), Nitrogen cycling in the Middle Atlantic Bight: Results from a three-dimensional model and implications for the North Atlantic nitrogen budget, *Global Biogeochem. Cycles*, *20*, GB3007, doi:10.1029/2005GB002456.

Gan, J., and J. S. Allen (2002), A modeling study of shelf circulation off northern California in the region of the Coastal Ocean Dynamics Experiment: Response to relaxation of upwelling winds, *J. Geophys. Res.*, *107*(C11), 3184, doi:10.1029/2001JC001190.

Gan, J., and J. S. Allen (2005), On open boundary conditions for a limited-area coastal model off Oregon. Part 2: Response to wind forcing from a regional mesoscale atmospheric model, *Ocean Modell.*, *8*(1–2), 155–173.

Gan, J., A. Cheung, X. G. Guo, and L. Li (2009a), Intensified upwelling over a widened shelf in the northeastern South China Sea, *J. Geophys. Res.*, *114*, C09019, doi:10.1029/2007JC004660.

Gan, J., L. Li, D. X. Wang, and X. G. Guo (2009b), Interaction of a river plume with coastal upwelling in the northeastern South China Sea, *Cont. Shelf Res.*, *29*(4), 728–740.

Harrison, P. J., K. D. Yin, J. H. W. Lee, J. P. Gan, and H. B. Liu (2008), Physical-biological coupling in the Pearl River Estuary, *Cont. Shelf Res.*, *28*(12), 1405–1415.

Hofmann, E., et al. (2008), Eastern US continental shelf carbon budget integrating models, data assimilation, and analysis, *Oceanography*, *21*(1), 86–104.

Huang, B. Q., W. L. Lan, Z. R. Cao, M. H. Dai, L. F. Huang, N. Z. Jiao, and H. S. Hong (2008), Spatial and temporal distribution of nanoflagellates in the northern South China Sea, *Hydrobiologia*, *605*, 143–157.

Li, K. Z., J. Q. Yin, L. M. Huang, and Y. H. Tan (2006), Spatial and temporal variations of mesozooplankton in the Pearl River estuary, China, *Estuarine Coastal Shelf Sci.*, *67*(4), 543–552.

Liu, K. K., S. Y. Chao, P. T. Shaw, G. C. Gong, C. C. Chen, and T. Y. Tang (2002), Monsoon-forced chlorophyll distribution and primary production in the South China Sea: Observations and a numerical study, *Deep Sea Res., Part I*, *49*(8), 1387–1412.

Liu, K. K., Y. J. Chen, C. M. Tseng, I. I. Lin, H. B. Liu, and A. Snidvongs (2007), The significance of phytoplankton photo-adaptation and benthic-pelagic coupling to primary production in the South China Sea: Observations and numerical investigations, *Deep Sea Res., Part II*, *54*(14–15), 1546–1574.

Lu, Z., J. Gan, M. Dai, and Y. Cheung (2010), The influence of coastal upwelling and a river plume on the subsurface chlorophyll maximum over the shelf of the northeastern South China Sea, *J. Mar. Syst.*, *82*, 35–46, doi:10.1016/j.jmarsys.2010.03.002.

Mellor, G. L., and T. Yamada (1982), Development of a turbulence closure-model for geophysical fluid problems, *Rev. Geophys.*, *20*(4), 851–875.

Ning, X., F. Chai, H. Xue, Y. Cai, C. Liu, and J. Shi (2004), Physical-biological oceanographic coupling influencing phytoplankton and primary production in the South China Sea, *J. Geophys. Res.*, *109*, C10005, doi:10.1029/2004JC002365.

Olson, R. J. (1981), Differential photoinhibition of marine nitrifying bacteria: A possible mechanism for the formation of the primary nitrite maximum, *J. Mar. Res.*, *39*(2), 227–238.

Parsons, T. R., Y. Maita, and C. M. Lalli (1984), *A Manual of Chemical and Biological Methods for Seawater Analysis*, 173 pp., Pergamon, Oxford, U. K.

Powell, T. M., C. V. W. Lewis, E. N. Curchitser, D. B. Haidvogel, A. J. Hermann, and E. L. Dobbins (2006), Results from a three-dimensional, nested biological-physical model of the California Current System and comparisons with statistics from satellite imagery, *J. Geophys. Res.*, *111*, C07018, doi:10.1029/2004JC002506.

Service, S. K., J. A. Rice, and F. P. Chavez (1998), Relationship between physical and biological variables during the upwelling period in Monterey Bay, CA, *Deep Sea Res., Part II*, *45*, 1669–1685.

Shchepetkin, A. F., and J. C. McWilliams (2005), The regional oceanic modeling system (ROMS): A split-explicit, free-surface, topography-following-coordinate oceanic model, *Ocean Modell.*, *9*(4), 347–404.

Song, Y. H., and D. Haidvogel (1994), A semiimplicit ocean circulation model using a generalized topography-following coordinate system, *J. Comput. Phys.*, *115*(1), 228–244.

Spitz, Y. H., J. S. Allen, and J. Gan (2005), Modeling of ecosystem processes on the Oregon shelf during the 2001 summer upwelling, *J. Geophys. Res.*, *110*, C10S17, doi:10.1029/2005JC002870.

Wu, J. F., S.-W. Chung, L.-S. Wen, K.-K. Liu, Y. L. Chen, H.-Y. Chen, and D. M. Karl (2003), Dissolved inorganic phosphorus, dissolved iron, and *Trichodesmium* in the oligotrophic South China Sea, *Global Biogeochem. Cycles*, *17*(1), 1008, doi:10.1029/2002GB001924.

Xu, J., K. Yin, L. He, X. Yuan, A. Ho, and P. Harrison (2008), Phosphorus limitation in the northern South China Sea during late summer: Influence of the Pearl River, *Deep Sea Res., Part I*, *55*, 1330–1342.

Xue, H., and F. Chai (2002), Coupled physical-biological model for the Pearl River Estuary: A phosphate limited subtropical ecosystem, in *Estuarine and Coastal Modeling: Proceedings of the Seventh International Conference, November 5–7, 2001, St. Petersburg, Florida*, edited by M. L. Spaulding, pp. 913–928, Am. Soc. of Civ. Eng., Reston, Va.

Yin, K. D. (2002), Monsoonal influence on seasonal variations in nutrients and phytoplankton biomass in coastal waters of Hong Kong in the vicinity of the Pearl River estuary, *Mar. Ecol. Prog. Ser.*, *245*, 111–122.

Yin, K. D., P.-Y. Qian, J. C. Chen, D. P. H. Hsieh, and P. J. Harrison (2000), Dynamics of nutrients and phytoplankton biomass in the Pearl River estuary and adjacent waters of Hong Kong during summer: Preliminary evidence for phosphorus and silicon limitation, *Mar. Ecol. Prog. Ser.*, *194*, 295–305.

Yin, K., X. Song, J. Sun, and M. Wu (2004), Potential P limitation leads to excess N in the Pearl River estuarine coastal plume, *Cont. Shelf. Res.*, *24*(16), 1895–1907.

Zhang, J., Z. G. Yu, J. T. Wang, J. L. Ren, H. T. Chen, H. Xiong, L. X. Dong, and W. Y. Xu (1999), The subtropical Zhujiang (Pearl River) Estuary: Nutrient, trace species and their relationship to photosynthesis, *Estuarine Coastal Shelf Sci.*, *49*(3), 385–400.

A. Y. Y. Cheung, P. Harrison, H. Liu, and Z. Lu, Division of Environment, Hong Kong University of Science and Technology, Clear Water Bay, Kowloon, Hong Kong. (ansoncyy@ust.hk; harrison@ust.hk; liuhb@ust.hk; luzm@ust.hk)

M. Dai, State Key Laboratory of Marine Environmental Science, Xiamen University, 422 Siming Nanlu, Xiamen 361005, China. (mdai@xmu.edu.cn)

J. Gan, Department of Mathematics, Hong Kong University of Science and Technology, Clear Water Bay, Kowloon, Hong Kong. (magan@ust.hk)